

## A Novel Approach for Accurate Estimation of the Growth Rate of the Detected Lung Nodules

Ayman El-Baz<sup>1</sup>, Georgy Gimel'farb<sup>2</sup>, Robert Falk<sup>3</sup>, David Heredia<sup>1</sup>, and Mohamed Abo El-Ghar<sup>4</sup>

<sup>1</sup>Bioimaging Laboratory, Bioengineering Department, University of Louisville, Louisville, KY, USA.

<sup>2</sup>Department of Computer Science, University of Auckland, Auckland, New Zealand.

<sup>3</sup>Director, Medical Imaging Division, Jewish Hospital, Louisville, KY, USA.

<sup>4</sup>Urology and Nephrology Department, University of Mansoura, Mansoura, Egypt.

**Abstract.** Our long term research goal is to develop a fully automated, image-based diagnostic system for early diagnosis of pulmonary nodules that may lead to lung cancer. This paper focuses on monitoring the development of lung nodules detected in successive chest low dose (LD) CT scans of a patient. We propose a new methodology for 3D LDCT data registration which is non-rigid and involves two steps: (i) global alignment of one scan (target) to another scan (reference or prototype) using the learned prior appearance model followed by (ii) local alignment in order to correct for intricate deformations. After equalizing signals for two subsequent chest scans, visual appearance of these chest images is modeled with a Markov-Gibbs random field with pairwise interaction. We estimate the affine transformation that globally register the target to the prototype by gradient descent maximization of a special Gibbs energy function. To handle local deformations, we deform each voxel of the target over evolving closed equi-spaced surfaces (iso-surfaces) to closely match the prototype. The evolution of the iso-surfaces is guided by an exponential speed function in the directions that minimize distances between the corresponding voxel pairs on the iso-surfaces in both the data sets. Preliminary results on the 135 LDCT data sets from 27 patients show that our proper registration could lead to precise diagnosis and identification of the development of the detected pulmonary nodules.

### 1 Introduction

Because lung cancer is the most common cause of cancer deaths, fast and accurate analysis of pulmonary nodules is of major importance for medical computer-aided diagnostic systems (CAD). We have already introduced the following three successive pre-processing stages of such a system: a fully automatic segmentation algorithm to separate lung regions from LDCT images [1], a fully automatic nodule detection algorithm showing the accuracy up to 93.3% on the experimental database containing 200 real LDCT chest data sets with 36,000 2D slices [3], and an accurate segmentation algorithm to separate the detected pulmonary nodules from the lung regions in the LDCT images [4]. This paper focuses on the next

stage, namely, on accurate registration of the detected nodules for subsequent volumetric measurements to monitor how the nodules are developing over the time.

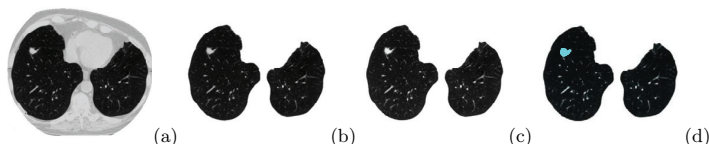


**Fig. 1.** Pre-processing steps: (a) an initial LDCT slice, (b) the segmented lung regions [1], (c) the normalized segmented lung regions, and (d) the segmented pulmonary nodules [4].

Figure 1 shows the results of the above-mentioned three pre-processing stages of the proposed CAD system for monitoring detected pulmonary nodules (these stages are not discussed in this paper): (*i*) an initial LDCT slice in Fig. 1(a) is segmented with the algorithms in [1] in order to isolate lung tissues from the surrounding structures in the chest cavity as shown in Fig. 1(b), (*ii*) data normalization as shown in Fig. 1(c), and (*iii*) the nodules in the isolated lung regions are segmented by evolving deformable boundaries under forces that depend on the learned current and prior appearance models as shown in Fig. 1(d) (see [4]). This paper focuses on details of the proposed global and local registration models being the core of our approach to monitoring the nodule development.

**Previous work.** Tracking the temporal nodule behavior is a challenging task because of changes in the patient’s position at each data acquisition, as well as effects of heart beats and respiration. In order to accurately measure how the nodules are developing in time, all these motions should be compensated by registering LDCT data sets taken at different time. Many methods have been proposed for solving medical image registration problems (see e.g. [5]) and to exclude the lung motions (see [6]). Moreover, it has been reported that the computer-assisted volume measurement is more reliable for small pulmonary nodules than the measurement by human experts [7]. Therefore, the remaining principal difficulty in monitoring and evaluating the nodule growth rate is automatic identification (or registration) of corresponding nodules in the follow-up scans. Registration of the two successive CT scans determines transformation of one image with respect to the other [8]. Some examples of previous works on registration of CT lung images are overviewed below.

Most of them exploit corresponding local structural elements (features) in the images. For the follow-up of small nodules, Brown et al. [9] developed a patient-specific model with 81% success for 27 nodules. Ko et al. [10] used centroids of local structures to apply rigid and affine image registration with 96% success for 58 nodules of 10 patients. To account for non-rigid motions and deformations of the lung, Woods et al. [11] developed an objective function using an anisotropic smoothness constraint and a continuous mechanical model. Feature points required by this algorithm are detected and registered as explained

in [12], and then the continuous mechanical model is used to interpolate the image displacement. In the Wood's experiments, the difference between the estimated and actual volumes was about 1.6%. Later on, Dougherty et al. [13] developed an optical flow and model based motion estimation technique for estimating first a global parametric transformation and then local deformations of the images. This method aligned sequential CT images with a 95% correlation. Naqa et al. [14] combined the optical flow analysis with spirometric data (measurements of the airflow into and out of lungs) in order to track the breathing motion automatically. The spirometry in this study was obtained by using the reconstruction of free breathing from the 4D CT data proposed in [15].

In several studies CT lung images are matched directly for pulmonary registration. Zhang et al. [16] used a standard lung atlas to analyze the pulmonary structures in CT images. The atlas is registered to a new image by combining global rigid and local elastic transformations of a 3D surface. Li et al. [17] still used feature points to search for correspondence but exploited landmark and intensity based registration algorithms to warp a template image to the rest of the lung volumes. Okada et al. [18] proposed an anisotropic intensity model fitting with analytical parameter estimation to evaluate the nodule volume without explicit image segmentation. Zhao et al. [19] and Kostis et al. [20] proposed to segment 2D and 3D nodules by thresholding the voxel intensity followed by a connectivity filter. Their algorithms accurately segment well-defined solid nodules with similar average intensities but become unreliable on cavities or non-solid nodules. Reeves et al. [21] proposed a framework for measuring changes of the nodule size from two CT scans recorded at different times. This approach is based on using rigid registration to align the scans followed by adaptive thresholding to segment the nodules.

Nonetheless, all the existing computational methods for monitoring the pulmonary nodules detected in the CT scans do not account for large deformations of the lung tissues due to breathing and heart beating. These methods are not suitable for some types of pulmonary nodules such as cavities and ground glass nodules. Also, these methods require significant user interaction which is difficult for a clinical practitioner.

**Our approach** to nodule monitoring is simpler for the clinical use because all the computations to follow up the pulmonary nodules detected in the LDCT images are performed fast and in a fully automatic mode. To achieve the goal of early diagnosis of malignant nodules, our system follows up the detected pulmonary nodules using the following image analysis steps:

1. location of the nodule either by an expert (radiologist) or using our previous lung CAD system [3];
2. segmentation of the lung in the LDCT images;
3. registration (global and local alignment) of two successive LDCT scans to correct motion artefacts caused by breathing and other patient motions and establish correspondence between the nodules;
4. segmentation of the corresponding pulmonary nodules; and

5. measurement of volumetric changes between the corresponding nodules.

## 2 Lung Motion Correction Models

### 2.1 Global Alignment

**Basic notation.** Let  $\mathcal{Q} = \{0, \dots, Q-1\}$ ;  $\mathbf{R} = [(x, y, z) : x = 0, \dots, X-1; y = 0, \dots, Y-1; z = 0, \dots, Z-1]$ , and  $\mathbf{R}_p \subset \mathbf{R}$  be a finite set of scalar image signals (e.g. gray levels), a 3D arithmetic lattice supporting digital LDCT image data  $g : \mathbf{R} \rightarrow \mathcal{Q}$ , and an arbitrary-shaped part of the lattice occupied by the prototype, respectively. Let a finite set  $\mathcal{N} = \{(\xi_1, \eta_1, \zeta_1), \dots, (\xi_n, \eta_n, \zeta_n)\}$  of the  $(x, y, z)$ -coordinate offsets define neighboring voxels, or neighbors  $\{((x + \xi, y + \eta, z + \zeta), (x - \xi, y - \eta, z - \zeta)) : (\xi, \eta, \zeta) \in \mathcal{N}\} \wedge \mathbf{R}_p$  interacting with each voxel  $(x, y, z) \in \mathbf{R}_p$ . The set  $\mathcal{N}$  yields a 3D neighborhood graph on  $\mathbf{R}_p$  that specifies translation invariant pairwise interactions between the voxels with  $n$  families  $\mathcal{C}_{\xi, \eta, \zeta}$  of second-order cliques  $c_{\xi, \eta, \zeta}(x, y, z) = ((x, y, z), (x + \xi, y + \eta, z + \zeta))$ . Interaction strengths are given by a vector  $\mathbf{V}^T = [\mathbf{V}_{\xi, \eta, \zeta}^T : (\xi, \eta, \zeta) \in \mathcal{N}]$  of potentials  $\mathbf{V}_{\xi, \eta, \zeta}^T = [V_{\xi, \eta, \zeta}(q, q') : (q, q') \in \mathcal{Q}^2]$  depending on signal co-occurrences; here T indicates transposition.

**Data normalization:** To account for possible monotone (order -preserving) changes of signals (e.g. due to different sensor characteristics), every LDCT data set is equalized using the cumulative empirical probability distribution of its signals (see Fig. 1(c)).

**MGRF based appearance model:** In a generic MGRF with multiple pairwise interaction [1], the Gibbs probability  $P(g) \propto \exp(E(g))$  of an object  $g$  aligned with the prototype  $g^\circ$  on  $\mathbf{R}_p$  is specified with the Gibbs energy  $E(g) = |\mathbf{R}_p| \mathbf{V}^T \mathbf{F}(g)$  where  $\mathbf{F}^T(g)$  is the vector of scaled empirical probability distributions of signal co-occurrences over each clique family:  $\mathbf{F}^T(g) = [\rho_{\xi, \eta, \zeta} \mathbf{F}_{\xi, \eta, \zeta}^T(g) : (\xi, \eta, \zeta) \in \mathcal{N}]$  where  $\rho_{\xi, \eta, \zeta} = \frac{|\mathcal{C}_{\xi, \eta, \zeta}|}{|\mathbf{R}_p|}$  is the relative size of the family and  $\mathbf{F}_{\xi, \eta, \zeta}^T(g) = [f_{\xi, \eta, \zeta}(q, q') : (q, q') \in \mathcal{Q}^2]^T$ ; here,  $f_{\xi, \eta, \zeta}(q, q') = \frac{|\mathcal{C}_{\xi, \eta, \zeta; q, q'}(g)|}{|\mathcal{C}_{\xi, \eta, \zeta}|}$  are empirical probabilities of signal co-occurrences, and  $\mathcal{C}_{\xi, \eta, \zeta; q, q'}(g) \subseteq \mathcal{C}_{\xi, \eta, \zeta}$  is a subfamily of the cliques  $c_{\xi, \eta, \zeta}(x, y, z)$  supporting the co-occurrence  $(g_{x, y, z} = q, g_{x+\xi, y+\eta, z+\zeta} = q')$  in  $g$ . The co-occurrence distributions and the Gibbs energy for the object are determined over  $\mathbf{R}_p$ , i.e. within the prototype boundary after an object is affinely aligned with the prototype. To account for the affine transformation, the initial image is resampled to the back-projected  $\mathbf{R}_p$  by interpolation.

The appearance model consists of the neighborhood  $\mathcal{N}$  and the potential  $\mathbf{V}$  to be learned from the prototype.

**Learning the potentials:** The MLE of  $\mathbf{V}$  is proportional in the first approximation to the scaled centered empirical co-occurrence distributions for the prototype [1]:

$$\mathbf{V}_{\xi,\eta,\zeta} = \lambda \rho_{\xi,\eta,\zeta} \left( \mathbf{F}_{\xi,\eta,\zeta}(g^\circ) - \frac{1}{Q^2} \mathbf{U} \right); (\xi, \eta, \zeta) \in \mathcal{N} \quad (1)$$

where  $\mathbf{U}$  is the vector with unit components. The common scaling factor  $\lambda$  is also computed analytically; it is approximately equal to  $Q^2$  if  $Q \gg 1$  and  $\rho_{\xi,\eta,\zeta} \approx 1$  for all  $(\xi, \eta, \zeta) \in \mathcal{N}$ . In our case it can be set to  $\lambda = 1$  because the registration uses only relative potential values and energies.

**Learning the characteristic neighbors:** To find the characteristic neighborhood set  $\mathcal{N}$ , the relative Gibbs energies  $E_{\xi,\eta,\zeta}(g^\circ) = \rho_{\xi,\eta,\zeta} \mathbf{V}_{\xi,\eta,\zeta}^\top \mathbf{F}_{\xi,\eta,\zeta}(g^\circ)$  for the clique families, i.e. the scaled variances of the corresponding empirical co-occurrence distributions, are compared for a large number of possible candidates.

To automatically select the characteristic neighbors, we consider an empirical probability distribution of the energies as a mixture of a large “non-characteristic” low-energy component and a considerably smaller characteristic high-energy component:  $P(E) = \pi P_{\text{lo}}(E) + (1 - \pi) P_{\text{hi}}(E)$ . Both the components  $P_{\text{lo}}(E)$ ,  $P_{\text{hi}}(E)$  are of arbitrary shape and thus are approximated with linear combinations of positive and negative discrete Gaussians (efficient EM-based algorithms introduced in [1] are used for both the approximation and the estimation of  $\pi$ ).

**Appearance-based registration:** The desired affine transformation of an object  $g$  corresponds to a local maximum of its relative energy  $E(g_{\mathbf{a}}) = \mathbf{V}^\top \mathbf{F}(g_{\mathbf{a}})$  under the learned appearance model  $[\mathcal{N}, \mathbf{V}]$ . Here,  $g_{\mathbf{a}}$  is the part of the object image reduced to  $\mathbf{R}_{\mathbf{p}}$  by the 3D affine transformation  $\mathbf{a} = [a_{11}, \dots, a_{23}]$ :  $x' = a_{11}x + a_{12}y + a_{13}z + a_{14}$ ;  $y' = a_{21}x + a_{22}y + a_{23}z + a_{24}$ ;  $z' = a_{31}x + a_{32}y + a_{33}z + a_{34}$ . The initial transformation step is a pure translation with  $a_{11} = a_{22} = 1$ ;  $a_{12} = a_{21} = 0$ , ensuring the most “energetic” overlap between the object and prototype. In other words, the chosen initial position  $(a_{14}^*, a_{24}^*, a_{34}^*)$  maximizes the Gibbs energy. Then the gradient search for the local energy maximum closest to the initialization selects all the 12 parameters  $\mathbf{a}$ .

Figures 2(c,d) show the results of the global alignment of two segmented lungs. It is clear from Fig. 2(d) that the global alignment is not perfect due to local deformation.

## 2.2 Local motion model

To handle local deformations, we propose to deform the object over evolving closed equi-spaced surfaces (distance iso-surfaces) so that it closely matches the prototype. The evolution is guided by an exponential speed function and intends to minimize distances between corresponding voxel pairs on the iso-surfaces in

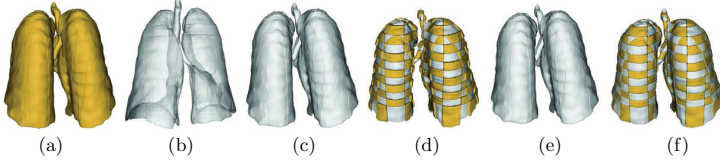


**Fig. 2.** 3D global and local registration: (a) reference data, (b) target data, (c) target data after 3D affine transformation, (d) checkerboard visualization to show the motion of lung tissues, (e) results of our non-rigid registration, and (f) checkerboard visualization to show the quality of the proposed local deformation model.

both the images. The normalized cross correlation of the Gibbs energy is used to find correspondences between the iso-surfaces.

Our approach involves the following steps. First, a distance map inside the object is generated using fast marching level sets [22]. Secondly, the distance map is used to generate iso-surfaces (Fig. 3). Note that the number of iso-surfaces is not necessarily the same for both the images and depends on the accuracy and the speed required by the user. The third step consists in finding correspondences between the iso-surfaces using the normalized cross correlation of the Gibbs energy. Finally, the evolution process deforms the iso-surfaces in the first data set (the target image) to match the iso-surfaces in the second data set (the prototype). The following notation is used below for defining the evolution equation:

- $\mathbf{b}_{\mathbf{g}_1}^h = [\mathbf{p}_k^h : k = 1, \dots, K]$  –  $K$  control points on a surface  $h$  on the reference data such that  $\mathbf{p}_k = (x_k, y_k, z_k)$  form a circularly connected chain of line segments  $(\mathbf{p}_1, \mathbf{p}_2), \dots, (\mathbf{p}_{K-1}, \mathbf{p}_K), (\mathbf{p}_K, \mathbf{p}_1)$ ;
- $\mathbf{b}_{\mathbf{g}_2}^\gamma = [\mathbf{p}_n^\gamma : n = 1, \dots, N]$  –  $N$  control points on a surface  $\gamma$  on the target data such that  $\mathbf{p}_n = (x_n, y_n, z_n)$  form a circularly connected chain of line segments  $(\mathbf{p}_1, \mathbf{p}_2), \dots, (\mathbf{p}_{N-1}, \mathbf{p}_N), (\mathbf{p}_N, \mathbf{p}_1)$ ;
- $S(\mathbf{p}_k^h, \mathbf{p}_n^\gamma)$  – the Euclidean distance between a point on the surface  $h$  in the image  $\mathbf{g}_1$  and the corresponding point on the surface  $\gamma$  in the image  $\mathbf{g}_2$ ;
- $S(\mathbf{p}_n^\gamma, \mathbf{p}_{n-1}^\gamma)$  – the Euclidean distance between a point on the surface  $\gamma$  in the image  $\mathbf{g}_1$  and the nearest point on the surface  $\gamma - 1$  in  $\mathbf{g}_1$ , and
- $\nu(\cdot)$  – the propagation speed function.

The evolution  $\mathbf{b}_\tau \rightarrow \mathbf{b}_{\tau+1}$  of a deformable boundary  $\mathbf{b}$  in discrete time,  $\tau = 0, 1, \dots$ , is specified by the system  $\mathbf{p}_{n,\tau+1}^\gamma = \mathbf{p}_{n,\tau}^\gamma + \nu(\mathbf{p}_{n,\tau}^\gamma) \mathbf{u}_{n,\tau}$ ;  $n = 1, \dots, N$  of difference equations where  $\nu(\mathbf{p}_{n,\tau}^\gamma)$  is a propagation speed function for the control point  $\mathbf{p}_{n,\tau}^\gamma$  and  $\mathbf{u}_{n,\tau}$  is the unit vector along the ray between the two corresponding points. The propagation speed function

$$\nu(\mathbf{p}_{n,\tau}^\gamma) = \min \{ S(\mathbf{p}_k^h, \mathbf{p}_{n,\tau}^\gamma), S(\mathbf{p}_{n,\tau}^\gamma, \mathbf{p}_{n,\tau}^{\gamma-1}), S(\mathbf{p}_{n,\tau}^\gamma, \mathbf{p}_{n,\tau}^{\gamma+1}) \}$$

satisfies the condition  $\nu(\mathbf{p}_{n,\tau}^\gamma) = 0$  if  $S(\mathbf{p}_k^h, \mathbf{p}_{n,\tau}^\gamma) = 0$  and prevents the current point from cross-passing the closest neighbor surfaces. The latter restriction is known as the smoothness constraint.

Again, the checkerboard visualization (Fig. 2(d)) of the data set in Fig. 2(a) and the aligned data set in Fig. 2(c) highlights the effect of the motion of lung tissues. It can be seen that the connections at the lung edges between the two volumes are not smooth when using only the global registration model. This is due to the local deformation which comes from breathing and heart beats. The connections of the lung edges between the two volumes are considerably smoother when using the proposed local deformation model (see Fig. 2(f)).

**Validation of the proposed local deformation model:** To validate the local registration, we simulated local deformations on the real LDCT data set using the free form deformation (FFD) [23] (it simulates local displacement with the 3D cubic spline). To measure the accuracy of the proposed local registration, three different types of the deformation fields were generated with the FFD: (1) small deformation, (2) moderate deformation, and (3) large deformation as shown in Table 1. Our registration model has been applied to each type of deformation, and the accuracy of our approach has been quantitatively assessed by comparing the simulated and recovered voxel displacements (see Table 1).

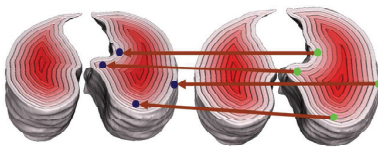


Fig. 3. Equi-spaced surfaces.

Table 1. Registration accuracy for simulated displacements (all units in mm).

|                               | Simulated displacement |               |               |
|-------------------------------|------------------------|---------------|---------------|
|                               | Type 1                 | Type 2        | Type 3        |
| Maximum displacement          | 1.7                    | 10.8          | 19.9          |
| Mean $\pm$ standard deviation | $0.6 \pm 0.4$          | $2.3 \pm 0.7$ | $9.1 \pm 1.1$ |
|                               | Alignment error        |               |               |
| Maximum error                 | 0.6                    | 1.4           | 2.1           |
| Mean $\pm$ standard deviation | $0.4 \pm 0.3$          | $1.0 \pm 0.4$ | $1.2 \pm 1.6$ |

### 3 Experimental Results

The proposed registration models were tested on the clinical datasets collected from 27 patients. Each patient has five LDCT scans, with the three months period between each two successive scans. This preliminary clinical database was collected by the LDCT scan protocol using a multidetector GE Light Speed Plus scanner with the following scanning parameters: slice thickness of 2.5 mm reconstructed every 1.5 mm, scanning pitch 1.5, pitch 1 mm, 140 KV, 100 MA, and F.O.V 36 cm.

After the two volumes at different time instants are registered, the task is to find out if the nodules are growing or not. For this purpose, the lung nodules were segmented after registration using our previous approach [4]. Once the nodules

are segmented in the original and the registered image sequences, the volumes of the nodules are calculated using the  $\Delta x$ ,  $\Delta y$ , and  $\Delta z$  values from the scanner (in our case, 0.7, 0.7, and 2.5 mm, respectively). Figure 4 shows the estimated growth rate for the two detected pulmonary nodules (for two different patients over one year) before and after data alignment.

| Patient #1       |                |                |                |                 |
|------------------|----------------|----------------|----------------|-----------------|
| Scanning periods | After 3 months | After 6 months | After 9 months | After 12 months |
| Before Alignment |                |                |                |                 |
| $\Delta V$       | 7.91%          | 28.7%          | 49.2%          | 121.9%          |
| After Alignment  |                |                |                |                 |
| $\Delta V$       | 27.3%          | 68.9%          | 113.5%         | 151.9%          |
| Patient #2       |                |                |                |                 |
| Scanning periods | After 3 months | After 6 months | After 9 months | After 12 months |
| Before Alignment |                |                |                |                 |
| $\Delta V$       | 0.96%          | 1.7%           | 5.71%          | 8.9%            |
| After Alignment  |                |                |                |                 |
| $\Delta V$       | 0.14%          | 0.81%          | 1.12%          | 1.79%           |

**Fig. 4.** Results of our registration for two patients over one year.

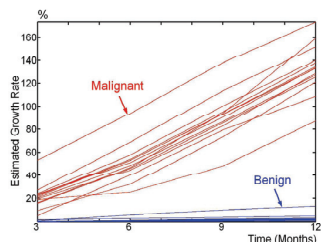


**Fig. 5.** Estimated volumetric changes for 14 malignant and 13 benign nodules.

It is clear that our alignment algorithm facilitates accurate evaluations of temporal changes in the nodule size. Moreover, the proposed alignment would help doctors and radiologists to track the nodule growth direction which is crucial for surgical or radiation treatment. Also, it is apparent that the malignant nodule doubles in size for 360 (or less) days, while the volumetric changes in the benign nodule are very small (maximum 6% over one year, see Figure 5).

Our statistical analysis using the unpaired  $t$ -test shows that the difference between the average growth rate of malignant nodules and the average growth rate of benign nodules found with the proposed approach is statistically significant (as shown in Table 2). Also, Table 2 shows that no significant difference is found if the growth rate is measured without the data alignment step. Figure 5 shows volumetric changes for 14 malignant and 13 benign nodules. It is obvious that the growth rate of the malignant nodules is considerably higher than the growth rate of the benign nodules, and this encourages to use the estimated growth rate as a discriminatory feature.

A traditional Bayes classifier based on the analysis of the growth rate of both benign and malignant nodules for 27 patients diagnosed 14 and 13 patients as malignant and benign, respectively. For simplicity, this classifier used a multivariate Gaussian model of the growth rate with the rates at 3, 6, 9, and 12 months as four discriminant features. The same patients were diagnosed by biopsy (the ground truth) showing that the classification was 100% correct. Therefore, the



**Table 2.** Growth rate statistics for 14 patients with malignant nodules and 13 patients with benign nodules ( $p$  – statistical significance;  $\mu$  – average rate, %;  $\sigma$  – standard deviation, %).

| Scanning period | With the proposed registration |            |         |            |           | Without the registration |            |         |            |     |
|-----------------|--------------------------------|------------|---------|------------|-----------|--------------------------|------------|---------|------------|-----|
|                 | Malignant                      |            | Benign  |            | $p$       | Malignant                |            | Benign  |            | $p$ |
|                 | $\mu_M$                        | $\sigma_M$ | $\mu_B$ | $\sigma_B$ |           | $\mu_M$                  | $\sigma_M$ | $\mu_B$ | $\sigma_B$ |     |
| 3 months        | 22                             | 16         | 0.9     | 0.7        | $10^{-4}$ | 5.6                      | 4.8        | 2.8     | 1.9        | 0.1 |
| 6 months        | 49                             | 20         | 2.9     | 2.3        | $10^{-4}$ | 11                       | 6.6        | 8.4     | 5.1        | 0.3 |
| 9 months        | 91                             | 29         | 4.5     | 3.8        | $10^{-4}$ | 24                       | 9.3        | 17      | 11         | 0.1 |
| 12 months       | 140                            | 32         | 5.4     | 4.3        | $10^{-4}$ | 30                       | 11         | 20      | 16         | 0.1 |

proposed image analysis techniques could be a promising supplement to the current technologies for diagnosing lung cancer.

## 4 Conclusions

We introduced a new approach for registering 3D spiral LDCT images that combines an initial affine global alignment of one scan (the target) to another scan (the reference) using the learned prior appearance model and subsequent local alignments that account for more intricate deformations. Preliminary results on 27 patients show the registration could lead to accurate diagnosis and identification of temporal development of detected pulmonary nodules. Our present C++ implementation on the Intel dual processor (3GHz each) with 8 GB memory and 1.5 TB hard drive with RAID technology takes about 330 sec for processing 182 LDCT slices of size 512×512 pixels each, i.e about 1.8 sec per slice. Our future work will focus on testing the proposed approach on more diverse data sets. We have already started to collect the data from additional 200 patients with different types of pulmonary nodules (e.g., ground glass, cavity, etc), in order to better measure the accuracy and limitations of the proposed framework.

**Acknowledgement:** This research work was supported in part by a grant from the Kentucky Science and Engineering Foundation as per Grant Agreement # KSEF-1645-RDE-011 with the Kentucky Science and Technology Corporation.

## References

1. A. Farag, A. El-Baz, and G. Gimel'farb, "Precise Segmentation of Multi-Modal Images," *IEEE Transactions on Image Processing*, vol. 15, no. 4, pp. 952–968, 2006.
2. A. El-Baz, "Novel Stochastic Models for Medical Image Analysis," *Ph.D. dissertation, University of Louisville*, Louisville, KY, Chapter 5, pp. 115–150, 2006.
3. A. Farag, A. El-Baz, and G. Gimel'farb, "Quantitative Nodule Detection in Low Dose Chest CT Scans: New Template Modeling and Evaluation for CAD System Design," *Proc. Int. Conf. on Medical Image Computing and Computer-Assisted Intervention (MICCAI'05)*, Palm Springs, California, USA, October 26–29, 2005, pp. 720–728, 2005.

4. A. El-Baz, et al., "A Framework for Automatic Segmentation of Lung Nodules from Low Dose Chest CT Scans", *Proc. IAPR Int. Conf. on Pattern Recognition (ICPR'06)*, Hong Kong, August 20–24, 2006, vol. 3, pp. 611–614, 2006.
5. J. Maintz and M. Viergever, "A Survey of Medical Image Registration," *Journal of Medical Image Analysis*, vol. 2, pp. 1–36, 1998.
6. J. Ko and D. Naidich, "Computer-Aided Diagnosis and the Evaluation of Lung Disease," *Journal of Thoracic Imaging*, vol. 19, no. 3, pp. 136–155, 2004.
7. W. Kostis, et al., "Small Pulmonary Nodules: Reproducibility of Three-Dimensional Volumetric Measurement and Estimation of Time to Follow-Up CT," *Radiology*, vol. 231, no. 2, pp. 446–452, May 2004.
8. B. Horn, "Closed-Form Solution of Absolute Orientation using Unit Quaternions," *Journal of the Optical Society of America B*, vol. 4, no. 4, pp. 629–642, 1987.
9. M. Brown, et al., "Method for Segmenting Chest CT Image Data using an Anatomical Model: Preliminary Results," *IEEE TMI*, vol. 16, no. 6, pp. 828–839, 1997.
10. J. Ko, and M. Betke, "Chest CT: Automated Nodule Detection and Assessment of Change over Time-Preliminary Experience," *Radiology*, vol. 218, pp. 267–273, 2001.
11. K. Woods, et al., "Model Supported Image Registration and Warping for Change Detection in Computer-Aided Diagnosis," *Applied Imagery Pattern Recognition (AIPR) Annual Workshops*, Washington DC, 2000.
12. L. Fan and C. Chen, "An Integrated Approach to 3D Warping and Registration from Lung Images," *Proceedings of SPIE Conf. Developments in X-Ray Tomography II*, July 1999.
13. L. Dougherty, et al., "Alignment of CT Lung Volumes with an Optical Flow Method," *Academic Radiology*, vol. 10, no. 3, pp. 249–254, 2003.
14. I. Naqa, et al., "Automated Breathing Motion Tracking for 4D Computed Tomography," *Nuclear Science Symp. Conference Record*, vol. 5, pp. 3219–3222, 2003.
15. D. Low, et al., "A Method for the Reconstruction of Four-Dimensional Synchronized CT Scans Acquired During Free Breathing," *Medical Physics*, vol. 30, pp. 1254–1263, 2003.
16. L. Zhang and J. Reinhardt, "3D Pulmonary CT Image Registration with a Standard Lung Atlas," *Proc. SPIE Conf. Medical Imaging*, vol. 4322, pp. 67–77, 2000.
17. B. Li, et al., "3-D Inter-Subject Warping and Registration of Pulmonary CT Images for a Human Lung Model," *Proc. SPIE Conf. on Medical Imaging*, vol. 4683, pp. 324–335, San Diego, CA, 2002.
18. K. Okada, et al., "Robust Anisotropic Gaussian Fitting for Volumetric Characterization of Pulmonary Nodules in Multislice CT," *IEEE TMI*, vol. 24, no. 3, pp. 409–423, 2005.
19. B. Zhao, et al., "Two-Dimensional Multicriterion Segmentation of Pulmonary Nodules on Helical CT Images," *Medical Physics*, vol. 26, pp. 889–895, 1999.
20. W. Kostis, et al., "Three-Dimensional Segmentation and Growth-Rate Estimation of Small Pulmonary Nodules in Helical CT Images," *IEEE TMI*, vol. 22, pp. 1259–1274, 2003.
21. A. Reeves, et al., "On Measuring the Change in Size of Pulmonary Nodules," *IEEE TMI*, vol. 25, no. 4, pp. 435–450, 2006.
22. J. Sethian, "Fast Marching Level Set Method for Monotonically Advancing Fronts," *Proc. National Academy of Sciences, USA*, vol. 93, pp. 1591–1595, Feb. 1996.
23. D. Rueckert, et al., "Nonrigid Registration using Freeform Deformations: Application to Breast MR Images," *IEEE TMI*, vol. 18, no. 8, pp. 712–721, 1999.